Journal of Power Sources 195 (2010) 1667–1675

Contents lists available at ScienceDirect

Journal of Power Sources

journal homepage: www.elsevier.com/locate/jpowsour

In situ-polymerized wicks for passive water management in proton exchange membrane fuel cells

Daniel G. Strickland, Juan G. Santiago*

Stanford University, Stanford, CA 94025, United States

ARTICLE INFO

Article history:
Received 13 July 2009
Received in revised form
14 September 2009
Accepted 15 September 2009
Available online 23 September 2009

Keywords:
PEM fuel cell
Water management
Water transport
Wick
Parallel channel
Flooding

ABSTRACT

Air-delivery is typically the largest parasitic loss in PEM fuel cell systems. We develop a passive water management system that minimizes this loss by enabling stable, flood-free performance in parallel channel architectures, at very low air stoichiometries. Our system employs *in situ*-polymerized wicks which conform to and coat cathode flow field channel walls, thereby spatially defining regions for water and air transport. We first present the fabrication procedure, which incorporates a flow field plate geometry comparable to many state-of-the-art architectures (e.g., stamped metal or injection molded flow fields). We then experimentally compare water management flow field performance versus a control case with no wick integration. At the very low air stoichiometry of 1.15, our system delivers a peak power density of 0.68 W cm^{-2}. This represents a 62% increase in peak power over the control case. The open channel and manifold geometries are identical for both cases, and we demonstrate near identical inlet-to-outlet cathode pressure drops at all fuel cell operating points. Our water management system therefore achieves significant performance enhancement without introducing additional parasitic losses.

1. Introduction

Presently, the transportation sector relies on petroleum for 95% of total energy used. As a result, transportation accounts for a considerable portion of global greenhouse gas emissions (24% in 2004). [1] Over the past decade, increased research and development has gone toward transportation technologies which exploit alternative energy sources. These technologies include bio fuel combustion, hybrid, plug-in hybrid, electric, and fuel cell vehicles. Of these technologies, market penetration models and technological advancement forecasts suggest that fuel cell vehicles may have the most promise for long-term CO_2 emission reduction [2,3]. Key disadvantages remain, however, which prevent near-term implementation and deployment of fuel cell vehicles. Some disadvantages include current cost of catalyst materials and manufacture, long-term durability issues, and the necessity of a fueling infrastructure [2,4].

Proton exchange membrane (PEM) fuel cells are favored for transportation due to their high efficiency, low operating temperature, and high power density [5]. A persistent challenge in PEM fuel cell systems, however, is water management [6]. Membrane humidity must be maximized to ensure good ionic conductivity [7], while excess product water must be removed to prevent electrode, gas diffusion layer (GDL), and flow field channel flooding [6]. Flooding has multiple impacts on fuel cell performance. At the very least, flooding reduces gas permeability in the GDL and, in effect, the limiting current [8–10]. In addition to GDL flooding, flow field channel flooding can lead to mal-distribution of reagent delivery, localized fuel starvation, and significant spatial non-uniformity in reaction rates [11–14]. These flooding events not only introduce large efficiency losses, but also lead to electrode and long-term performance degradation [4]. Flooding poses additional challenges in stacks, where cell flow fields are manifolded in parallel. In such systems, flooding in a single cell has minimal impact on overall inlet-to-outlet pressure drop. As a result, product water can continue to accumulate. This leads to non-uniformity in cell-to-cell potentials, and, in severe cases, cell reversal [15].

Effective water management, therefore, is critical for stable and long-term reliable performance [16,17]. This is often addressed by using fully humidified inlet gas streams and incorporating serpentine channel cathode flow fields for air-delivery [18]. The long channel length and reduced air channel cross-sectional area of serpentine designs lead to increased pressure drop and increased air velocities, which advectively remove excess product water. Although stable performance is achieved, this approach results in large parasitic power losses (as high as 35% of stack power) and increased system complexity [18–20]. Required auxiliary compressor and gas humidification systems also reduce power density through increased system size, sometimes accounting for up to 20% of total fuel cell system volume [21].

Parallel channel cathode flow field architectures are appealing, as they require minimal pressure differentials to deliver

* Corresponding author at: 440 Escondido Mall, Bldg 530, Rm 225, Stanford, CA 94025, United States. Tel.: +1 650 723 5689; fax: +1 650 723 7657.
E-mail address: juan.santiago@stanford.edu (J.G. Santiago).

0378-7753/$ – see front matter © 2009 Elsevier B.V. All rights reserved.
doi:10.1016/j.jpowsour.2009.09.034

reactants. They offer reduced air compression and delivery parasitic power. These architectures are often impractical, however, as they typically require high stoichiometric air-flow rates to achieve flood-free, stable performance [13,22].

Several groups have proposed novel methods to minimize air stoichiometry requirements while maintaining effective water management. We here first review largely passive and then active water management strategies. Voss et al. removed excess product water through the anode by enforcing a cathode-to-anode membrane water saturation gradient [23]. This saturation gradient was realized through careful control of anode and cathode gas humidification. In another study, Inoue et al. developed cooling water channel designs to strategically impose thermal gradients, and by extension, saturation pressure gradients. This resulted in approximately uniform relative humidity [24]. Similarly, Li et al. leveraged in-channel pressure gradients to maintain gas streams precisely at saturation [18]. As air pressure decreases with distance downstream, water carrying capacity increases. Li et al. used this effect to develop a simple cathode channel design model which matches increased water carrying capacity with water production rate. Although these methods have shown effective water management, they significantly constrain system design and geometry, and are often not compatible with parallel channel, low-pressure differential, flow field designs.

An alternative approach is to use active flood mitigation for parallel flow field architectures. Yi et al. employed hydrophilic, porous carbon water transport plates as cell separators [25]. These water transport plates remain fully saturated and internally humidify undersaturated gas streams, while a pressure differential applied between gas and internal water transport channels removes excess product water. Buie et al. integrated an electroosmotic (EO) pump directly into a fuel cell cathode [26] and applied an electric field to drive liquid water from the GDL to an external reservoir. Litster et al. extended this idea by externally coupling an EO pump with a porous carbon cathode flow field [27,28]. In their design, an EO pump generated pressure gradient removed excess product water absorbed by the porous carbon flow field. These active water management strategies all enabled stable, flood-free performance in parallel channel flow field architectures, at significantly reduced air stoichiometries.

Although both passive and active water management strategies have resulted in considerable performance enhancements, concerns remain related to fuel cell cost, manufacturability, and power density, specifically in the transportation sector. Separator plates typically account for 80% of stack weight and a significant portion of the total stack cost. State-of-the-art separator plates leverage injection molding or stamping manufacture procedures to minimize cost and weight [29]. To the best of our knowledge, current flood mitigation techniques are very difficult to integrate into these new flow field designs, specifically those which utilize parallel channels. In the present work, we develop a passive water management system that enables stable performance in parallel channel flow field designs at extremely low air stoichiometries, and can be integrated with state-of-the-art flow field architectures. We leverage an *in situ*-polymerized wick design which can conform to the shape of existing flow field plates and be used to provide water management while minimizing pressure drop.

2. Material and methods

2.1. Water management flow field design overview

We *in situ*-polymerized 200 μm thick polymer wicks on the channel walls of a 19 parallel channel 25 cm^2 aluminum flow field. The wick is created and integrated using a novel photopolymerization and molding process which we detail in Section 2.2. The wick spatially defines regions for water (wick) and air (open channel) transport. The channel wick is contiguous with a thin "wick header" molded into the top surface of the outlet manifold. This wick header is 150 μm thick and also connects hydraulically to the outside of the fuel cell via a separate porous wick "bridge" which, when saturated, allows water transport while maintaining a gas seal. The wick bridge is 47 mm wide, and made from glass filter cloth (Whatman GF/D, UK). The integrated, *in situ*-polymerized wicks are hydrophilic. We measured a contact angle of ∼55° on a non-porous polymer sample (made using the same chemistry and procedure but without adding porogen chemical) using a contact angle analyzer (FTA200, First Ten Angstroms, Portsmouth, VA). The wick structure in the channels therefore initially absorbs liquid product water once it emerges from the GDL. Wick capillary pressure, defined as the surface tension induced difference between gas and liquid pressures, decreases from a maximum value at low water saturations (where only the smallest pores are filled) to zero when the wick is fully saturated. Therefore, capillary forces initially redistribute water by inducing liquid pressure gradients which transport water from high to low saturation regions.

Once the wick is fully saturated, capillary pressure becomes negligible and liquid and gas pressure gradients likely become equal. This is because even a small amount of liquid water on the wick surface is enough to prevent menisci on the wick surface from supporting a wick-to-channel pressure difference (see Litster et al. [28] for further discussion of wick capillary pressures and wick-to-channel pressure differences). As a result, and as per Darcy's law [30], axial in-channel air pressure gradients induce water flow downstream within channel wicks and to the wick header in the outlet manifold. Excess product water then either travels out through the gas outlet or through the wick bridge via a slight pressure difference between the outlet manifold and ambient. Consistent with discussion by Litster et al. [28], we assume full wick saturation during steady-state operation. Therefore, in effect, wicks provide a liquid water transport pathway from reaction sites to outside of the fuel cell by leveraging air pressure gradients.

Fig. 1 shows the passive cathode water management flow field (WMFF) design. Our control (no wick) flow field is shown in the inset. We fabricated both flow fields to have approximately identical open flow areas in both channels and manifold. This resulted in nearly identical inlet-to-outlet pressure drops for both the wick and no wick cases. Carefully controlling geometry is important, as pressure drop and air velocities relate directly to water removal rate and air compressor parasitic power. We note that the wick material is a dielectric polymer. As a result, the WMFF has a reduced conducting area in contact with the GDL. Conductive rib thicknesses are 370 and 670 μm for the WMFF and control, respectively. Current interrupt measurements revealed a slight increase in area specific resistance, from 100.5 to 101.0 mΩ cm^2 (a difference smaller than the uncertainty of our impedance measurements). For all cases, we used a triple serpentine anode flow field to prevent anode-side flooding.

2.2. Fabrication procedure

2.2.1. Injection molding

In this section, we describe the molding process used to fabricate wicks on the surface of the cathode water management flow field. We first precision end-milled aluminum (McMaster-Carr, Chicago, IL) flow fields for both the water management (wick) and control (no wick) cases. We machined the water management flow field to have channel and manifold dimensions 150 μm larger to allow room for subsequent polymerization of surface mounted wicks. We then used a solvent resistant, polyester resin (TAP Plastics, Mountain View, CA) to cast the top "negative image" mold for injection molding. The control flow field plate itself served as the casting

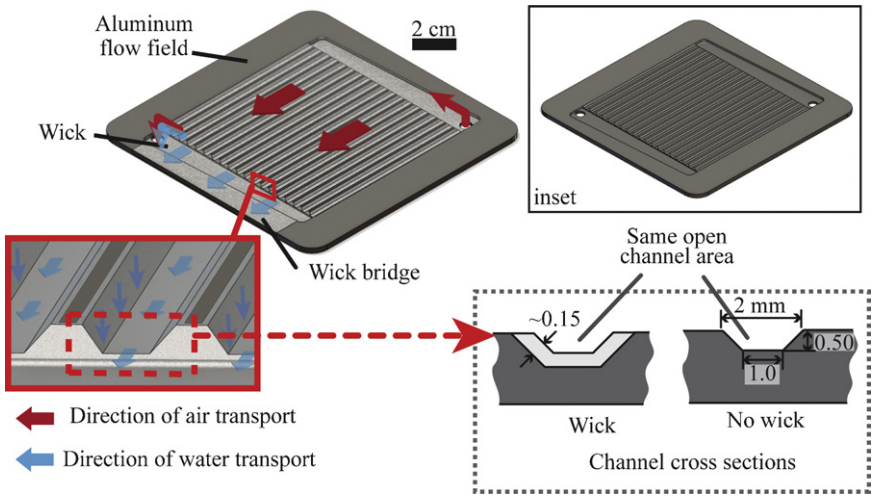

Fig. 1. Passive water management flow field (WMFF) design. The main image (top left) and a detail view (bottom left) show the aluminum flow field with integrated wick. Control (no wick) flow field is shown in the inset on the top right. The cross-section of the wick and control case are compared on the bottom right. Both flow fields have equal open channel and manifold geometry to ensure similar gas flow characteristics. ~150 μm thick polymer wicks coat the channel and manifold surfaces of the WMFF. Channel wicks absorb liquid product water ejected from the GDL. Initially, capillary forces distribute water throughout the wick structure. Once fully saturated, in-channel gas pressure gradients induce in-wick pressure gradients and flow of water downstream. Water travels through channel wicks to a wick header in the outlet manifold. Excess product water then leaves the fuel cell through the gas outlet or through the wick bridge, via a slight pressure difference between outlet manifold and ambient.

template for the wick mold to ensure nearly identical open channel geometry of the finished flow field. We note that by leveraging the difference between the control and water management flow field geometries for injection molding, we achieved precisely defined wick geometry. See the Supplementary Information document for more details.

Fig. 2 shows details of the wick fabrication procedure. We assembled the top mold, the water management flow field, a silicone gasket, and a Teflon support plate, using eight 10-32 bolts for compression. Using a glass syringe, we then injected a solution of monomers, solvents, and photo-initiator (chemistry detailed in Section 2.2.2) via luer-lock ports on the back side of the mold assembly, and visually confirmed that the solution displaced all air in voids between the aluminum flow field and top mold. We then sealed the mold and photo-initiated polymerization with a UV-light source (~365 nm peak) for 1 h. During polymerization, the monomer solution turned from transparent to opaque and resulted in a porous polymer monolith. We then removed the flow field from the mold, and soaked it in several baths of methanol for a total of 12 h. To prevent oxide-layer formation and potential ion contamination of the fuel cell, we subsequently electroplated both the water management and control flow fields with a 10 μm nickel diffusion barrier and then 1 μm gold (Electrochem, Union City, CA). The electroplating left the porous polymer wick surface intact.

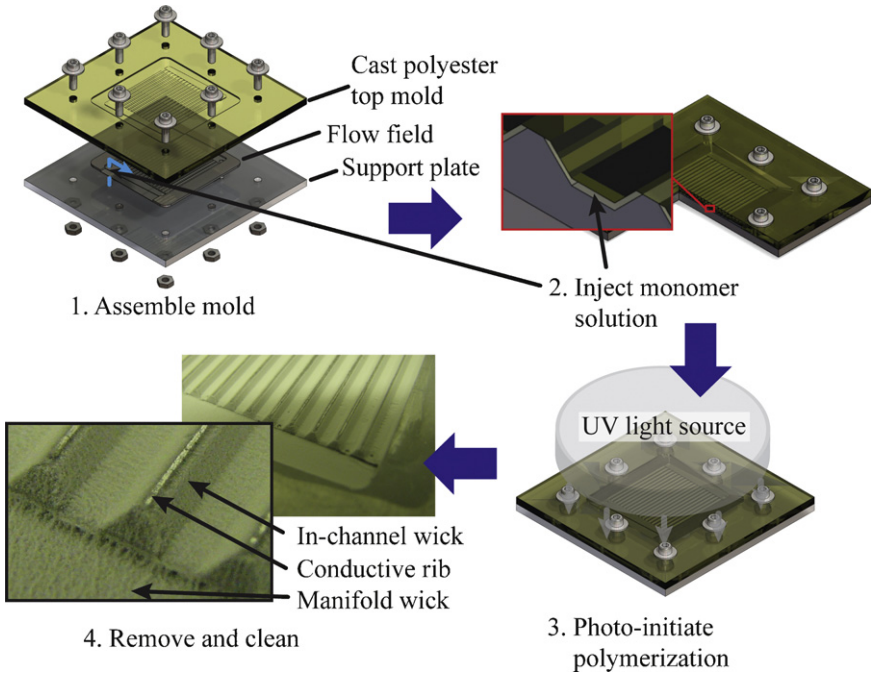

Fig. 2. Injection molding procedure for WMFF: we (1) assembled the mold, which includes top "negative image" mold, flow field plate, silicone gasket (not shown) and Teflon support plate; (2) injected monomer solution to fill voids between flow field plate and top mold; (3) sealed mold and photo-initiated polymerization with UV-light source for 1 h; and (4) removed and cleaned in a methanol bath.

2.2.2. In situ polymerization of porous materials

We provide here a brief description of the reagents, reactions, and processing of the polymerization procedure. We will present a more detailed discussion (and comparison with alternate chemistries) in a future paper. Porous polymers are fabricated by combining monofunctional and crosslinking monomers with a solution of porogenic solvents in a closed mold. For the chemistry used here, we use a photo-initiator to carry out free radical polymerization. As polymer chain length increases, the polymer becomes insoluble. As a result, a two-phase system of solid polymer and liquid solvent forms. For sufficiently high monomer concentrations, polymer globules join together and a porous monolith results. Pore size distribution and porosity of the resulting monolith are influenced by four parameters: solubility of monomers in the chosen solvent mixture, ratio of monofunctional to crosslinking monomers, ratio of total monomers to total solvent, and the rate of reaction (influenced by initiator concentration, temperature, and UV-light source intensity).

Fig. 3 shows the chemistry we used for the WMFF wicks. We adapted this chemistry from work published by Yu et al. [31]. We used monomers of ethylene glycol dimethylacrylate (EDMA – CAS# 97-90-5) for crosslinking and 2-hydroxyethyl methacrylate (HEMA – CAS# 868-77-9) for hydrophilic functionality, a binary solvent system of methanol (MeOH) and hexane (Hex), and benzoin methyl ether (CAS# 3524-62-7) for photo initiation. We achieved a maximum permeability of 2.65×10^{-12} m^2 using monomer:solvent, HEMA:EDMA, and MeOH:Hex volumetric ratios of 3:7, 1:1, 3:2, respectively, and 1.25 wt% initiator. The preparation procedure was as follows. We passed EDMA and HEMA through a column packed with an inhibitor remover (Sigma–Aldrich prod # 311332), and then degassed all reagents by bubbling nitrogen gas for 7 min. We then combined reagents in a scintillation vial according to the desired volumetric ratios and respective densities, using a precision scale (Pinnacle PI-225D, Denver Instrument, Denver, CO). Finally, we bubbled nitrogen gas through the solution for 3 min to further reduce oxygen concentration in solution. We then injected this solution into the mold, as described in Section 2.2.1.

2.3. Fuel cell assembly

Fuel cell assembly and experimental setup is similar that reported by Litster et al. [28], and we only summarize it here. Fig. 4 shows fuel cell assembly used for all experiments. Starting at center and moving out, it consists of a membrane-electrode assembly (MEA), gas diffusion layers (GDLs), cathode and anode flow fields, current collectors, silicone layers for electrical insulation, and aluminum support plates for compression.

We used a commercially available catalyst coated membrane (Ion-Power, New Castle, DE) with membrane thickness of 25 μm and total Pt catalyst loading of 0.3 mg cm^{-2}. GDLs were Sigracet-10BB with a microporous layer. A 280 μm Teflon gasket, placed around each GDL, sealed gases and prevented over compression. We machined the anode flow field from graphite (fuelcellstore.com, Boulder, CO), and used a triple serpentine flow field with 0.75 mm square channels, and 0.75 mm land widths. The cathode flow field used is as described in Section 2.1. We machined current collectors from copper which we then electroplated with 1 μm gold (Electrochem, Union City, CA). Custom machined aluminum support plates and four 10-32 bolts, tightened to 15 in-lb, provided compression. For all experiments, we oriented the fuel cell horizontally and fed gases in counter flow.

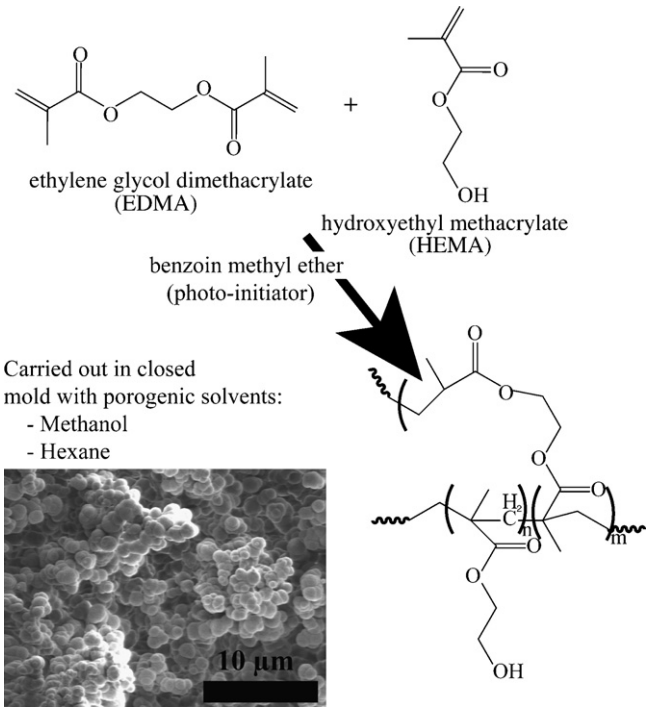

Fig. 3. Polymerization chemistry used for flow field wicks. We carried out a free radical polymerization of EDMA and HEMA in a sealed mold with methanol and hexane, using benzoin methyl ether as a photo-initiator. During polymerization, as molecule size increases, the polymers become insoluble. This results in a two-phase system of solid polymer and liquid solvents. For sufficiently high monomer concentrations, polymers join and form a continuous porous monolith. The inset shows a scanning electron micrograph (SEM) of the resulting structure.

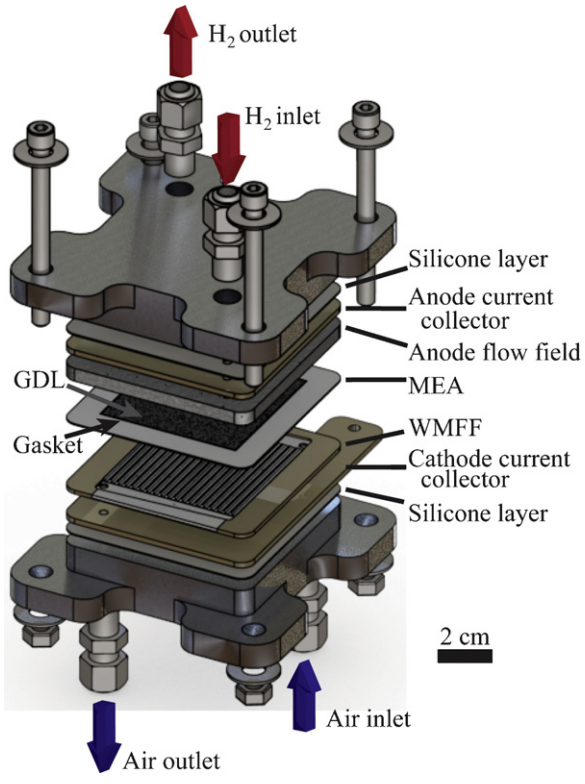

Fig. 4. Exploded view of 25 cm^2 fuel cell assembly. The fuel cell features the water management flow field (WMFF) on the cathode side and triple serpentine flow field on the anode. A commercially available catalyst coated membrane is sandwiched between two GDLs with microporous layers and Teflon gaskets for sealing. Custom machined support plates are electrically insulated from current collectors with a 500 μm silicone layer. Four bolts tightened to 15 in-lb provide compression. The assembly was oriented horizontally and gases were fed in counter flow in all experiments.

Table 1
Experimental parameters for both wick-integrated and control fuel cell systems.

Parameter	Value
Fuel cell temperature	65 °C
Cathode saturator temperature	65 °C
Anode saturator temperature	65 °C
Gas line temperature	75 °C
Hydrogen stoichiometry (α_{H_2})	1.5
Number of channels (cathode)	19
Active area	25 cm^2
MEA	Ion power CCM
GDL	Sigracet-10BB
Anode/cathode outlet pressure	1 atm (abs)

2.4. Experimental setup

Here, we briefly describe the setup used for all experiments. Cylinders of compressed air and hydrogen (Praxair) connected to electronic mass flow controllers (Alicat Scientific, Tucson, AZ), and then to a humidification system (Bekktech, Inc., Loveland, CO). Saturator temperature was set equal to fuel cell temperature to ensure full gas humidification. Heated tubes, with temperature 10 °C warmer than saturators to prevent condensation, connected the saturators to the fuel cell gas inlets. A temperature controller (Omega CSC32, Stamford, CT) set fuel cell temperature via two Kapton heaters (McMaster-Carr, Chicago, IL) fixed to fuel cell endplates and a K-type thermocouple which was embedded in the anode flow field plate. We used a pressure transducer at the cathode inlet to measure inlet-to-outlet pressure drop.

All experiments were controlled and data collected using Labview 8.5. We used an electronic load (Agilent N3301A, Palo Alto, CA) with power assist boost (Acopian W3.3MT65, Easton, PA) to galvanostatically control experiments. Air and hydrogen stoichiometry were fixed throughout each polarization curve. Prior to using each membrane, we used a voltage cycling procedure to break in the cell. In this break-in period, we cycled fuel cell voltage from 0.8, 0.5, to 0.3 V for 20 s each, for a total of 8 h. Table 1 lists key parameters used in all experiments.

3. Results and discussion

3.1. In-channel pressure gradients

In-channel pressure gradients and air velocities play a critical role in fuel cell water management, and more specifically, in channel flooding [11,32]. As a result, maintaining similar pressure drop characteristics for the control and water management flow field designs was necessary to isolate the effect of wick integration on water management. Fig. 5 shows normalized inlet-to-outlet pressure drop versus current density for both the control and water management flow field cases. Pressure is normalized by air stoichiometry, α_{air}, and plotted for $\alpha_{air} = 1.15$, 1.30, 1.50, and 2.0. As the figure shows, flow field hydraulic resistance is nearly identical for both the WMFF and control, and at all fuel cell operating points. Because hydraulic resistance is nearly equal, we therefore expect no additional air-delivery parasitic loss due to wick integration.

3.2. Water transport regime

We here first briefly review some multiphase water transport terms and physics, and then present and discuss our experimental results. In a detailed visualization study, Zhang et al. identified three regimes by which liquid product water is removed from the GDL surface [33]. By balancing surface adhesion and drag forces, Zhang derived a semi-empirical relation for droplet detachment size as a function of air velocity. As air velocity increases, the characteristic diameter of droplets at detachment decreases. For sufficiently high air velocities, droplets detach before contacting channel walls and advect as air-stream-borne droplets (a mist). At lower velocities, droplet detachment size becomes comparable to channel dimensions. For hydrophilic channel walls that satisfy the Concus–Finn condition [34], droplets join a corner flow upon contacting the channel wall. However, at high current densities, corner flow is unable to remove all product water; and this leads to annular film and eventual water slug formation.

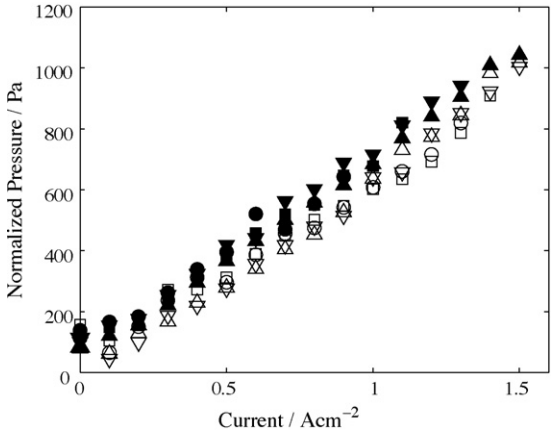

Fig. 5. Pressure normalized by stoichiometry vs. current density for control (closed) and WMFF (open) cases and stoichiometries of $\alpha_{air} = 1.15$ (○), 1.30 (□), 1.50 (▽), and 2.00 (△). The relationship between normalized pressure and current density is linear, indicating constant hydraulic resistance, regardless of current density or air stoichiometry. Both the control and WMFF approximately collapse to the same line, indicating nearly equal hydraulic resistance.

For the channel geometry used in the current study, the maximum average channel velocity was 1.5 m s^{-1} (at maximum air stoichiometry and current density of $\alpha_{air} = 2.0$ and $j = 1.5$ A cm^{-2}, respectively). At these velocities, detachment droplet characteristic dimension is expected to be larger than the channel. Also, channel surface properties and geometry are such that the Concus–Finn condition is not met, so corner flow is not sustained and we expect channel slug formation. Transient voltage yields insight into flooding events [28,32,35]. The data in Fig. 6 indeed suggest slug flow does occur. Fig. 6 shows representative realizations of fuel cell potential versus time during polarization curve measurements for both control and WMFF, at $\alpha_{air} = 1.3$. Here, the dynamic fuel cell load is adjusted to increment current density by 0.1 A cm^{-2} every 600 s. The inset details transient performance of the control flow field in the high current density regime (which is likely partially flooded). Voltage data reveal a characteristic fuel cell response, which involves a gradual decreases in performance followed by sudden, temporary recovery events. We hypothesize that this is due to gradual liquid water accumulation in the flow field channels and/or manifold. Once a critical liquid water content is reached, accumulated product water intermittently purges, and cell performance momentarily recovers.

3.3. Engineering model of gas pressure gradient-driven water transport in wicks

The WMFF case shows significant performance enhancement. The temporal fluctuations of voltage at each current setting are much lower than the control case. At most operating points, channel wicks likely transport enough product water along the wicks to successfully mitigate slug formation and catastrophic flooding. Using a simple Darcy flow model, we can estimate the fraction of product water that the measured pressure drop is capable of

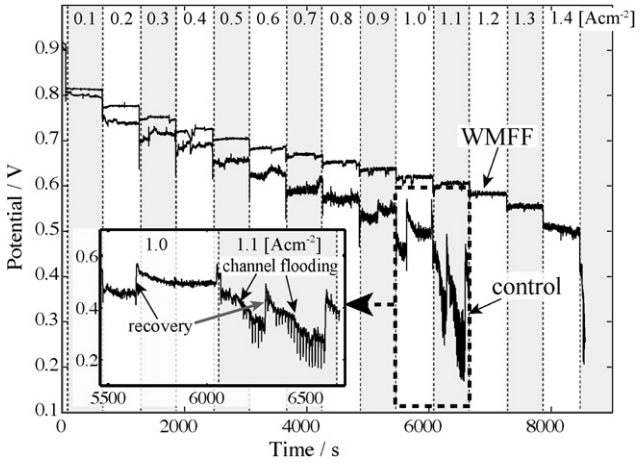

Fig. 6. Representative voltage versus time for polarization curve measurements at $\alpha_{air} = 1.3$, for control and WMFF cases. Cell current was increased by 0.1 A cm^{-2} every 600 s. Data indicate significant performance degradation due to flooding in the control case. Voltage transients (inset) show performance decline and discrete events of partial recovery. These transients are consistent with liquid water accumulation in channels and manifold, followed by spontaneous, intermittent purging. The WMFF shows significantly improved performance. WMFF data reveal stable performance for most current densities. Low magnitude voltage fluctuations, however, suggest some liquid water may also be present in channels, particularly at low current densities (j = 0.3–0.4 A cm^{-2}) and again at the highest current density (j = 1.4 A cm^{-2}). In this wick case, failure occurred suddenly and immediately after incrementing current to 1.5 A cm^{-2}.

transporting through the channel wicks. We estimate the maximum water flow rate in the wick as

$$Q_{wick,max} = \frac{A_w}{\mu_{H_2O}} k_w \frac{\Delta P}{L_c}, \quad (1)$$

where A_w is the channel wick cross-sectional area, μ_{H_2O} is the dynamic viscosity of water, k_w is the wick permeability, ΔP is the measured pressure drop from inlet-to-outlet, and L_c is the channel length. We measured k_w *ex situ*, using a specially fabricated porous monolith sample and the radial flow method [36,37] (these calibrations used the same polymer chemistry reported in Section 2.2.2). This expression slightly over-estimates pressure induced flow in the wick, as the measured inlet-to-outlet pressure difference is not dropped over the channel length alone (but includes difficult-to-quantify manifold and interconnect losses).

We can normalize $Q_{wick,max}$ by the water production rate to obtain a measure of the fraction of product water transported by the wick:

$$\chi = \frac{Q_{wick,max}}{Q_{prod}}, \quad (2)$$

where the volumetric water production rate is $Q_{prod} = (jA_{fc}/2Fn_{chan})(M_{H_2O}/\rho_{H_2O})$, where A_{fc} is the fuel cell active area, F is faraday's constant, n_{chan} is the number of channels, and M_{H_2O} and ρ_{H_2O} are the density and molar mass of water, respectively.

Fig. 7 shows a plot of χ versus α_{air}. We obtained this data by first analyzing χ versus current density, j, for stoichiometries of α_{air} = 1.15, 1.30, 1.50, and 2.0 (shown in inset). We calculated χ using Eqs. (1) and (2), and pressure data measured during polarization curve experiments (which we present in Section 3.5). As the inset shows, for each stoichiometry, χ is roughly independent of current density as expected for relatively flood-free channels. We obtain the main plot of Fig. 7 by averaging χ for $j > 0.5$ A cm^{-2} (shown in dashed box) for each stoichiometry.[1]

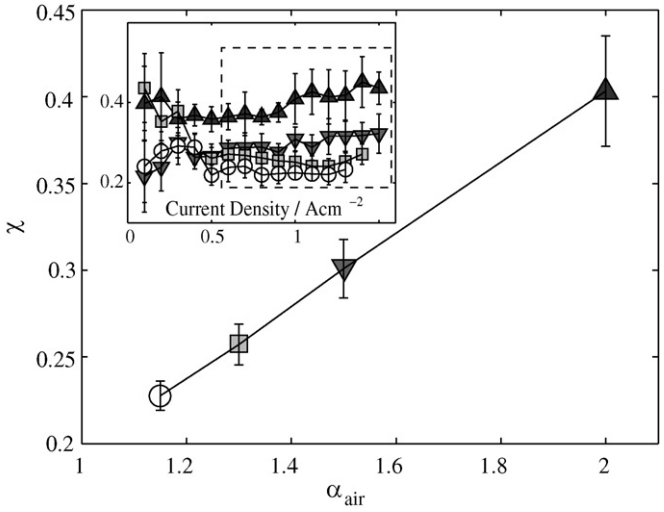

Fig. 7. Maximum fraction of product water transported through wick by measured pressure drop, χ, for stoichiometries of α_{air} = 1.15 (○), 1.30 (□), 1.50 (▼), and 2.00 (▲). The inset shows χ vs. current density for each stoichiometry. Error bars represent the standard deviation of temporal fluctuations in χ. We averaged values of χ for $j > 0.5$ A cm^{-2} (dashed box) to obtain each data point in the main figure. Results indicate that, for stoichiometric flow rates considered, channel wicks transport at most 41% of product water.

Results suggest that χ is independent of current density and increases linearly with air stoichiometry. This functional relationship is expected and can be elucidated by rewriting ΔP in Eq. (1). We recall from Fig. 5 that ΔP had an approximately linear dependence on flow rate. This suggests that in our experiments, cathode gases remained in a laminar pipe-flow regime. We therefore rewrite ΔP as:

$$\Delta P = R_{chan}\left(\alpha_{air}\frac{jA_{fc}}{4Fn_{chan}}\frac{M_{air}}{\rho_{air}}\right), \quad (3)$$

where R_{chan} is the effective channel hydraulic resistance and the term in brackets is the approximate air-flow rate per channel. We substitute ΔP, $Q_{wick,max}$, and Q_{prod} into Eq. (2) to obtain a new relation for χ:

$$\chi = \left(\frac{R_{chan}}{R_w}\right)\left(\frac{\rho_{H_2O}}{\rho_{air}}\frac{M_{air}}{M_{H_2O}}\right)\frac{\alpha_{air}}{2}, \quad (4)$$

where we define a wick hydraulic resistance as $R_w = \mu_{H_2O}L_c/k_wA_w$. In the current study, geometric parameters (first set of brackets) and fluid thermophysical parameters (second set of brackets) remain constant. Eq. (4) is therefore consistent with the experimental results for $j > 0.5$ A cm^{-2} as shown in Fig. 7. In effect, water transport in the wick automatically responds to increase in Q_{prod}, as both water production and air pressure drops each scale proportionally with air-flow rate.

As Eq. (4) indicates, aside from thermophysical fluid properties, three main parameters govern χ: R_{chan}, R_w, and α_{air}. Increasing R_{chan} and α_{air} enhances through wick water transport. However, either of such increases also increases air pressure drop, resulting in additional parasitic power. Parasitic power increase can be avoided by instead minimizing R_w. For our system, k_w, A_w, and L_c are 2.65×10^{-12} m^2, 7.50×10^{-5} m^2, and 5 cm, respectively. Using these values, results shown in Fig. 7 indicate that, for the air stoichiometries considered, the channel wicks likely do not transport

[1] In this averaging, we neglect $j \leq 0.5$ A cm^{-2} data, as two-phase flow physics dominate pressure measurements in this range. Non-linearities introduced by two-phase fluctuations are not accounted for in our model, and are most prominent in the low current density regime for two reasons. First, flood induced channel shutdown is substantial at the low air-flow rates encountered at low current density. Such shutdown results in large changes in system hydraulic resistance. Second, the low current regime is more susceptible to noise in χ, as we normalize $Q_{wick,max}$ by Q_{prod}.

all produced water. For example, we estimate that channel wicks transport only 41% of product water at the highest air stoichiometry of $\alpha_{air} = 2.0$. In future flow field designs, increasing either channel wick cross-sectional area or permeability would increase this flow fraction.

Complete characterization of secondary water transport mechanisms is not the intent of this study, and would require a more in-depth visualization study. We hypothesize, however, that corner and/or annular film flow carries a significant fraction of produced water. This is supported by the voltage data we present in Fig. 6. For $j = 0.3–0.4\ A\,cm^{-2}$, slight voltage fluctuations suggest some liquid water may accumulate in the flow field. At higher current densities, however, these transients disappear and performance appears flood-free. Adequate liquid water removal rate at higher current densities could be accounted for by a transition to corner/annular film flow. Such a regime transition is expected when increasing gas superficial velocity [38], as is the case when incrementing to higher current density.

3.4. Vapor-phase transport of water

Lastly, we note the effect of vapor-phase transport of water. In all our experiments, we set saturator temperature equal to fuel cell temperature to ensure full gas humidification. For high current density operation ($j > 1.2\ A\,cm^{-2}$), however, temperature near the membrane (measured with thermocouple embedded in anode flow field) increased above the set point by up to 6 °C. We attribute this temperature increase to heat generated by reaction and charge transport losses. We therefore expect some evaporative water removal in the high current density region. For the worst-case scenario, where measured fuel cell temperature rose to 71 °C, we estimate evaporative removal is limited to less than 15% of produced water (maximum evaporation rate calculated for $j = 1.5\ A\,cm^{-2}$ and $\alpha_{air} = 2.0$). We expect negligible evaporation for $j \leq 1.2\ A\,cm^{-2}$, as the measured temperature remained at 65 °C.

3.5. Polarization curves

In this section, we present polarization curves for the control and water management flow field cases. Before each polarization curve, we operated the fuel cell at $0.8\ A\,cm^{-2}$ and $\alpha_{air} = 1.8$ for 10 min to ensure a repeatable start condition. We purged the cathode of any accumulated product water with an 1840 sccm air-flow rate for 10 s. We began each polarization curve experiment by measuring open circuit voltage for 1 min. We then incremented current by $0.1\ A\,cm^{-2}$ every 10 min and terminated the experiment once the instantaneous voltage dropped below 0.2 V. Each data point represents the time average of the last 2 min of each 10 min dwell period.

Fig. 8 shows polarization curves for the control and WMFF cases, for stoichiometries of $\alpha_{air} = 1.15$, 1.30, 1.50, and 2.0. In the control case, flooding affected performance at all stoichiometries. This was expected, as stoichiometries used were significantly less than those typically required for stable performance using parallel channel cathode flow fields [22]. Flooding was most pronounced in the very low stoichiometry cases. For $\alpha_{air} = 1.15$, 1.30, and 1.50, catastrophic flooding prevented operation above 0.9, 1.1, and $1.3\ A\,cm^{-2}$, respectively. Flooding is often associated with high current density operation ($j > 1\ A\,cm^{-2}$ [10,39]). However, we observed significant performance losses in the low current density region. This is consistent with previous work showing that, when both stoichiometry and current density are small, flooding can be pronounced [27,40] and lead to mass transport losses resulting from flow mal-distribution and reduced GDL permeability, and kinetic losses resulting from reduced effective active area. We therefore attribute low current density flooding to minimal

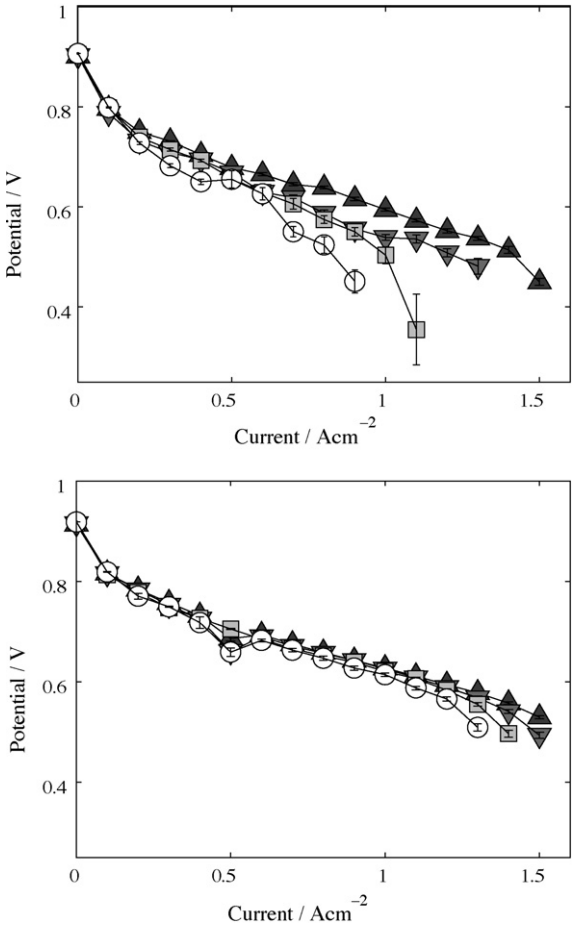

Fig. 8. Polarization curves for control (top) and WMFF (bottom) for $\alpha_{air} = 1.15$ (○), 1.30 (□), 1.50 (▼), and 2.00 (▲). Error bars represent ±1 standard deviation of temporal fluctuations in potential. For the control case, we observed pronounced flooding at all air stoichiometries. Flooding was most significant for $\alpha_{air} = 1.15–1.50$ and restricted the maximum obtainable current density. The WMFF demonstrated considerable performance improvement. For most operating points, performance appeared flood-free. An exception was in the mid-current density range ($j = 0.3–0.6\ A\,cm^{-2}$), where voltage transients suggested some water slug formation in channels.

water removal rates which result from low air-flow rates. Performance improved at the increased stoichiometry of $\alpha_{air} = 2.0$. Flooding appeared present at nearly all current densities, however, and was most significant in the high current density range. Voltage transients also suggested channel flooding, which eventually led to fuel cell failure.

The WMFF significantly improved fuel cell performance. Polarization curves revealed stable, flood-free performance at nearly all operating points. One exception was in the mid-current density range ($j = 0.3–0.6\ A\,cm^{-2}$), where voltage transients indicated some channel slug formation. Performance recovered, however, at increased current densities (and, by extension, increased air-flow rates) and appeared flood-free. The WMFF extended operating range by 0.4, 0.3 and $0.2\ A\,cm^{-2}$ for stoichiometries of $\alpha_{air} = 1.15$, 1.30 and 1.50, respectively. For each case, fuel cell failure occurred suddenly and immediately after incrementing current for the final time.

Results using the WMFF indicate that the system's degree of flooding does not increase monotonically with current density. As current is increased, fuel cell performance transitions from near open cell potential, through a short region of flooding, then through a significant region of recovery, and then finally a sudden catastrophic flooding event at termination. Possible factors causing the

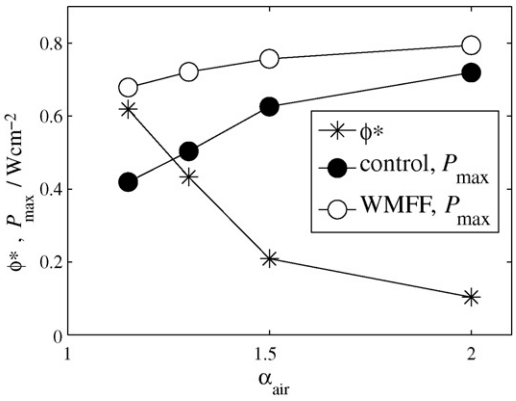

Fig. 9. Maximum power generated by the fuel cell (P_{max}) as a function of stoichiometry for control and WMFF cases (closed and open circles, respectively). We also plot the (non-dimensional ratio of) fractional power increase, ϕ^*, due to wick integration. The WMFF significantly increased P_{max} for all air stoichiometries, and especially for the low α_{air} cases. Results show a 62% increase in peak power for $\alpha_{air} = 1.15$. ϕ^* decreased with increasing α_{air}, from 0.62 at $\alpha_{air} = 1.15$ to 0.10 at $\alpha_{air} = 2.0$.

recovery phase include a change of water transport regime (e.g., slug to corner flow) or increased evaporative removal due to internal heating. Water transport and management is a delicate balance between production and removal, and deserves further investigation in future work. Visualization studies of our system are difficult but would perhaps further elucidate important water transport mechanisms. Other possible diagnostic tools for further investigation include neutron imaging [41–43], X-ray radiography [44], and magnetic resonance imaging [45] for water distribution measurements or cell segmentation methods to spatially resolve flooding events [12].

3.6. Power density performance

Fig. 9 shows maximum power density as a function of air stoichiometry for control and WMFF cases. As expected, maximum power increases with air-flow rate. At all soichiometries tested, wick integration significantly increased maximum power. This power increase was most significant at low stoichiometries. For example, the WMFF increased maximum power from 0.41 to 0.68 W cm^{-2} for $\alpha_{air} = 1.15$. To quantify performance enhancement, we also plot the fractional increase in max power, ϕ^*, which we define as:

$$\phi^* = \frac{P_{max,WMFF} - P_{max,control}}{P_{max,control}}. \quad (5)$$

As shown in Fig. 9, the WMFF increased max power by 62% at the lowest stoichiometry of $\alpha_{air} = 1.15$. ϕ^* decreased roughly as the inverse of air stoichiometry, diminishing to 10% at $\alpha_{air} = 2.0$. We again note that wick integration introduced no additional hydraulic resistance. Therefore, power measurements can be compared directly, as the WMFF introduced no additional parasitic losses.

4. Conclusions

We developed a passive water management cathode flow field that enabled stable, flood-free performance with 19 parallel channels at very low air stoichiometries. We presented a fabrication procedure where we *in situ* polymerize wicks on the flow field channel walls and manifold surfaces. This resulted in high quality, 150 μm thick, monolithic wick structures, which provided a hydraulically connected pathway from reaction sites to outside of the fuel cell. We used geometry and materials similar to many state-of-the-art flow field designs (e.g., stamped metal flow fields), and hypothesize that the water management system can be affordably integrated into transportation scale fuel cell stacks.

We experimentally compared fuel cell performance using the water management flow field (WMFF) against a control cathode flow field (no integrated wicks) which had identical open channel and manifold geometry. The WMFF significantly improved performance. For $\alpha_{air} = 1.15$, 1.30 and 1.50, the WMFF extended operating range by 0.4, 0.3 and 0.2 A cm^{-2}, respectively. Performance improvement was most significant for $\alpha_{air} = 1.15$. At this very low air stoichiometry, integrated wicks increased maximum power from 0.41 to 0.68 W cm^{-2}. This represents a 62% increase in peak power. At all operating points, inlet-to-outlet pressure drops were nearly identical for both the WMFF and control flow fields. Performance enhancements were therefore obtained without introducing additional air-delivery parasitic losses.

Even with the WMFF, we observed some mid-current density range flooding at all air stoichiometries. For the low air stoichiometries used, a simple model suggested that the wick alone does not transport all product water. Further investigation is therefore necessary to fully understand any secondary water transport mechanisms. Possible diagnostic tools include neutron imaging and cell segmentation for spatially resolved water content and reaction rates. In addition to identifying these transport mechanisms, ongoing work is focused on leveraging integrated wicks to enable high performance dry-gas operation. We are also working to couple wicks with a passive pre-humidification structure to maximize dry-gas fuel cell performance.

Acknowledgments

We gratefully acknowledge support from the Department of Defense under contract number W81XWH-07-1-0384 and the National Science Foundation for a Graduate Research Fellowship for Daniel G. Strickland. We also thank Frantisek Svec for very helpful comments and suggestions, initially teaching us about *in situ* polymerization, and access to his lab at the Lawrence Berkeley National Laboratory. We also thank Raquel Ponce and David Fenning for help in initial prototyping efforts of porous polymer samples.

Appendix A. Supplementary data

Supplementary data associated with this article can be found, in the online version, at doi:10.1016/j.jpowsour.2009.09.034.

References

[1] K. Ribeiro, S. Kobayashi, M. Beuthe, J. Gasca, D. Greene, D.S. Lee, Y. Muromachi, P.J. Newton, S. Plotkin, D. Sperling, R. Wit, P.J. Zhou, Climate Change 2007: Transport and its infrastructure, 2007.
[2] Transitions to Alternative Transportation Technologies—A Focus on Hydrogen, National Research Council, 2008.
[3] C. Thomas, International Journal of Hydrogen Energy 34 (15) (2009) 6005–6020.
[4] W. Schmittinger, A. Vahidi, Journal of Power Sources 180 (1) (2008) 1–14.
[5] G. Shimshon, A.Z. Tom, Advances in Electrochemical Science and Engineering (2008) 195–301.
[6] H. Li, Y. Tang, Z. Wang, Z. Shi, S. Wu, D. Song, J. Zhang, K. Fatih, J. Zhang, H. Wang, Z. Liu, R. Abouatallah, A. Mazza, Journal of Power Sources 178 (1) (2008) 103–117.
[7] T.A. Zawodzinski, C. Derouin, S. Radzinski, R.J. Sherman, V.T. Smith, T.E. Springer, S. Gottesfeld, Journal of the Electrochemical Society 140 (4) (1993) 1041–1047.
[8] C. Ziegler, T. Heilmann, D. Gerteisen, Journal of the Electrochemical Society 155 (4) (2008) B349–B355.
[9] A.Z. Weber, R.M. Darling, J. Newman, Journal of the Electrochemical Society 151 (10) (2004) A1715–A1727.
[10] U. Pasaogullari, C.Y. Wang, Journal of the Electrochemical Society 151 (3) (2004) A399–A406.
[11] L. Zhang, W. Du, H. Bi, D. Wilkinson, J. Stumper, H. Wang, Journal of Power Sources 189 (2) (2009) 1023–1031.
[12] D.G. Strickland, S. Litster, J.G. Santiago, Journal of Power Sources 174 (1) (2007) 272–281.

[13] Z. Lu, S. Kandlikar, C. Rath, M. Grimm, W. Domigan, A. White, M. Hardbarger, J. Owejan, T. Trabold, International Journal of Hydrogen Energy 34 (8) (2009) 3445–3456.
[14] F. Buchi, A.B. Geiger, R. Neto, Journal of Power Sources 145 (1) (2005) 62–67.
[15] T. Van Nguyen, M.W. Knobbe, Journal of Power Sources 114 (1) (2003) 70–79.
[16] J.R. Yu, T. Matsuura, Y. Yoshikawa, M.N. Islam, M. Hori, Physical Chemistry Chemical Physics 7 (2) (2005) 373–378.
[17] N. Yousfi-Steiner, P. Mocoteguy, D. Candusso, D. Hissel, A. Hernandez, A. Aslanides, Journal of Power Sources 183 (1) (2008) 260–274.
[18] X Li, I. Sabir, J. Park, Journal of Power Sources 163 (2) (2007) 933–942.
[19] D.P. Wilkinson, H.H. Voss, K. Prater, Journal of Power Sources 49 (1–3) (1994) 117–127.
[20] R.K. Ahluwalia, X. Wang, A. Rousseau, R. Kumar, Journal of Power Sources 130 (1–2) (2004) 192–201.
[21] F.N. Buchi, S. Srinivasan, Journal of the Electrochemical Society 144 (8) (1997) 2767–2772.
[22] W.R. Merida, G. McLean, N. Djilali, Journal of Power Sources 102 (1–2) (2001) 178–185.
[23] H.H. Voss, D.P. Wilkinson, P.G. Pickup, M.C. Johnson, V. Basura, Electrochimica Acta 40 (2) (1995) 321–328.
[24] G. Inoue, T. Yoshimoto, Y. Matsukuma, M. Minemoto, H. Itoh, S. Tsurumaki, Journal of Power Sources 162 (1) (2006) 94–104.
[25] J.S. Yi, J.D.L. Yang, C. King, AIChE Journal 50 (10) (2004) 2594–2603.
[26] C.R. Buie, J.D. Posner, T. Fabian, C.A. Suk-Won, D. Kim, F.B. Prinz, J.K. Eaton, J.G. Santiago, Journal of Power Sources 161 (1) (2006) 191–202.
[27] D. Strickland, S. Litster, J.G. Santiago, Journal of Power Sources 174 (1) (2007) 272–281.
[28] S. Litster, C.R. Buie, T. Fabian, J.K. Eaton, J.G. Santiago, Journal of the Electrochemical Society 154 (10) (2007) B1049–B1058.
[29] D.J.L. Brett, N.P. Brandon, Journal of Fuel Cell Science and Technology 4 (1) (2007) 29–44.
[30] L. Dake, Fundamentals of Reservoir Engineering, Elsevier, 1978.
[31] C. Yu, M. Xu, F. Svec, J.M.J. Frechet, Journal of Polymer Science: Part A Polymer Chemistry 40 (6) (2002) 755–769.
[32] X.G. Yang, F.Y. Zhang, A.L. Lubawy, C.Y. Wang, Electrochemical Solid State 7 (11) (2004) A408–A411.
[33] F.Y. Zhang, X.G. Yang, C.Y. Wang, Journal of the Electrochemical Society 153 (2) (2006) A225–A232.
[34] P. Concus, R. Finn, Proceedings of the National Academic Science of the United States of America 63 (2) (1969).
[35] J.P. Owejan, T.A. Trabold, J.J. Gagliardo, D.L. Jacobson, R.N. Carter, D.S. Hussey, M. Arif, Journal of Power Sources 171 (2) (2007) 626–633.
[36] H. Tan, K.M. Pillai, Journal of Composite Materials 43 (21) (2009) 2307–2332.
[37] K. Han, Composites Science and Technology 60 (12–13) (2000) 2435–2441.
[38] W.L. Chen, M.C. Twu, C. Pan, International Journal of Multiphase Flow 28 (7) (2002) 1235–1247.
[39] J.J. Baschuk, X.H. Li, Journal of Power Sources 86 (1–2) (2000) 181–196.
[40] K. Tuber, D. Pocza, C. Hebling, Journal of Power Sources 124 (2) (2003) 403–414.
[41] R. Satija, D.L. Jacobson, M. Arif, S.A. Werner, Journal of Power Sources 129 (2) (2004) 238–245.
[42] M.A. Hickner, N.P. Siegel, K.S. Chen, D.S. Hussey, D.L. Jacobson, M. Arif, Journal of the Electrochemical Society 155 (4) (2008) B427–B434.
[43] A. Turhan, K. Heller, J.S. Brenizer, M.M. Mench, Journal of Power Sources 180 (2) (2008) 773–783.
[44] C. Hartnig, I. Manke, R. Kuhn, S. Kleinau, J. Goebbels, J. Banhart, Journal of Power Sources 188 (2) (2009) 468–474.
[45] S. Tsushima, K. Teranishi, S. Hirai, Electrochemical Solid State 7 (9) (2004) A269–A272.